Multilayer interface tracking model of pure tungsten oxidation

Shu Huang[1], Ryan Kerr[2,3], Samuel Murphy[2], Mark R. Gilbert[3], Jaime Marian[1,4]

[1]Department of Materials Science and Engineering, University of California Los Angeles, Los Angeles, CA 90095, USA
[2]Engineering Department, Lancaster University, Bailrigg, Lancashire LA1 4YW, UK
[3]United Kingdom Atomic Energy Authority, Culham Centre for Fusion Energy, Culham Science Centre, Abingdon, Oxon OX14 3DB, UK
[4]Department of Mechanical and Aerospace Engineering, University of California Los Angeles, Los Angeles, CA 90095, USA

E-mail: jmarian@ucla.edu

July 2022

Abstract. We present a numerical model to predict oxide scale growth on tungsten surfaces under exposure to oxygen at high temperatures. The model captures the formation of four thermodynamically-compatible oxide sublayers, WO_2, $WO_{2.72}$, $WO_{2.9}$, and WO_3, on top of the metal substrate. Oxide layer growth is simulated by tracking the oxide/oxide and oxide/metal interfaces using a sharp-interface Stefan model coupled to diffusion kinetics. The model is parameterized using selected experimental measurements and electronic structure calculations of the diffusivities of all the oxide subphases involved. We simulate oxide growth at temperatures of 600°C and above, extracting the power law growth exponents in each case, which we find to deviate from classical parabolic growth in several cases. We conduct a comparison of the model predictions with an extensive experimental data set, with reasonable agreement at most temperatures. While many gaps in our understanding still exist, this work is a first attempt at embedding the thermodynamic and kinetic complexity of tungsten oxide growth into a comprehensive mesoscale kinetic model that attempts to capture the essential features of tungsten oxidation to fill existing knowledge gaps and guide and enhance future tungsten oxidation models.

Keywords: Tungsten oxide, High-temperature oxidation, Stefan model, Oxygen transport, Diffusion coefficients

1. Introduction

Corrosion of metallic structural materials is an extraordinarily broad phenomenon with implications in many areas of engineering [1–3]. In fusion energy devices, where tungsten (W) is the preferred candidate material for plasma-facing applications, the reaction chamber is designed to operate under nominal ($\approx 10^{-8}$ Torr) vacuum conditions [4–6]. However, under accident scenarios leading to a loss of cooling (LOCA) with simultaneous air ingress (due to loss of structural integrity of the vacuum chamber), W oxidizes rapidly, forming an unstable radioactive oxide that can break off mechanically and/or by sublimation, presenting a potentially-severe environmental hazard [7–9]. This has prompted the development of advanced tungsten alloys with enhanced oxidation resistance to eliminate the harmful release of toxic tungsten oxide into the environment in case of a LOCA event [10–12]. Good understanding of W oxidation rates is also needed to support the planning of execution of maintenance and decommissioning, where atmospheric control may be required to prevent the hazardous oxidation or the temperature may need careful control to restrict oxidation to more benign phases [13, 14]. As well, considerable interest in tungsten oxides stems from it use as a highly efficient hydrogen oxidation electrocatalyst [15].

While much progress has been made to understand the mechanisms of W oxidation in high temperature conditions [16–18], the inherent complexities associated with the coexistence of several different tungsten oxide phases make this topic one still under vigorous investigation. Under nominal conditions, W oxide structures experiences a series of transformations where temperature, stresses, and environmental conditions all play key roles in the evolution of the oxide scale. Cifuentes *et al* [19] have provided an excellent description of the overall oxidation process at high temperature, which is summarized as follows: "At 600°C, a protective $WO_{2.72}$ layer forms. This layer cracks at a prescribed thickness, leading to a rapid increase in mass gain resulting from fast oxygen transport through percolation pathways. The arrival of oxygen at the $WO_{2.72}$/metal interface turns the oxide into a coarse non-protective columnar $WO_{2.9}$ layer. The relative abundance of vacancies in $WO_{2.9}$ favors oxygen transport into the alloy, leading to rapid growth. Above

700°C, growth stresses in the scale are released through local cracking. At this stage, $WO_{2.9}$ becomes progressively transformed into WO_3 when the oxygen partial pressure increases across the scale thickness". As well, Lassner and Schubert [15] confirm that above 500°C the native $WO_{2.72}$ oxide layer cracks, and above 600°C turns into WO_3. WO_3 is permeable to oxygen, and its formation rate depends on the oxygen ion transport to the $WO_3/WO_{2.72}$ interface. So long as the $WO_{2.72}$ layer thickness stays below its critical value, the growth is parabolic, while –after it cracks– the growth turns to linear.

The fact that WO_{3-x} phases form below their equilibrium temperature threshold is likely related to the existence of compressive tangential stresses with a high Pilling-Bedworth ratio [20]. These stresses stabilize the oxide layer during the incipient growth phase but they build up with layer thickness, which ultimately results in loss of protection and cracking [21, 22]. The process described by Cifuentes *et al* and Lassner and Schubert does not involve the WO_2 phase. This could be caused by failure to achieve steady state during the length of time attained in experiments, or an inability to detect the WO_2 layer. Coexistence of WO_2 and WO_3 has been detected, however, under certain conditions [23]. The next stage of the oxidation process occurs when the WO_3 has covered the surface of the thin dark film. Being porous, not particularly adhesive and having a Pilling-Bedworth ratio of 3.35, this oxide creates high stresses causing the oxide layer to crack and thus exposing new surface to the oxygen. At this point, the non-protective nature of the WO_3 layer results in a linear oxidation rate.

Under loss-of-coolant or loss-of-vacuum conditions, air ingress and decay heat can push the temperatures in the tungsten between 1200 and 1500°C for several weeks [24]. At these temperatures, oxidation of pure W is almost immediate, and direct sublimation of WO_3 is then the main concern. The favored allotrope of WO_3 in this situation is the tetragonal (α) structure, with the rest of tungsten oxide phases becoming marginally stable and not observed [25].

Understandably, the multi-parametric nature and microstructural complexity of tungsten oxidation presents a difficult challenge for developing predictive material models and design guidelines. Recently, Nagy and Humphry-Baker have provided an oxidation mechanism map from an extensive compilation of experimental data [26]. These maps are an excellent visual tool to quickly determine the expected oxidation behavior of tungsten slabs as a function of temperature and time. However, unlike for oxidation of nuclear materials [20], there is a lack of fundamental models operating

at relevant scales to simulate oxide scale growth under a variety of conditions. In this work, we present a kinetic model of oxide interface evolution based on oxygen transport across a series of layers representing different oxide stoichiometries. The model is informed by equilibrium phase diagrams by furnishing the appropriate oxide phases at each thermodynamic condition. The model is parameterized with a combination of experimental and calculated material properties and physical constants. In particular, we carry out density functional theory (DFT) calculations of oxygen vacancy formation and migration energy barriers, as well as the attempt frequency in WO_2 to define the oxygen diffusivity in the corresponding layer.

The paper is organized as follows. First, a review of the physical-chemistry of W oxidation and a detailed description of the methods developed here are provided in Sec. 2. The results of the paper are presented in Sec. 3, including DFT calculations of diffusion parameters in WO_2 and simulations furnished by the model under several different scenarios. We provide a discussion of our findings in Sec. 4, and finish with the main conclusions of the paper in Sec. 5.

2. Methods

2.1. Preliminary considerations

Under high oxygen partial pressure conditions, the WO_3 layer grows by the transfer of mass from the metal represented by the reaction:

$$W^{6+} + 3O^{2-} \rightarrow WO_3 \tag{1}$$

This reaction is enabled by the reduction of molecular oxygen‡ on the environment side:

$$O_2 + 2e^- \rightarrow 2O^{2-} \tag{2}$$

which receives electrons from the oxidation of metal tungsten within the metal substrate:

$$W \rightarrow W^{6+} + 6e^- \tag{3}$$

The formation of WO_{3-x} phases follows the same sequence as above but with other oxidation states of tungsten as the starting point, such as +2, +3, +4, or +5.

‡ In aqueous conditions, the equivalent process is: $H_2O \rightarrow O^{2-} + 2H^+$

On the basis of these considerations, in the most general case the oxidation of metallic tungsten will evolve into a structure characterized by five distinct layers. These layers represent different tungsten-oxygen structures ranging from WO_3 on the environment side (where O radicals are produced) to the W-O metallic solid solutions (where the metal is reduced). In between, three more oxide phases are expected to form, namely, $WO_{2.9}$, $WO_{2.72}$, and WO_2. More details about the structure and properties of the different oxide compounds can be found in Appendix A.1. As shown

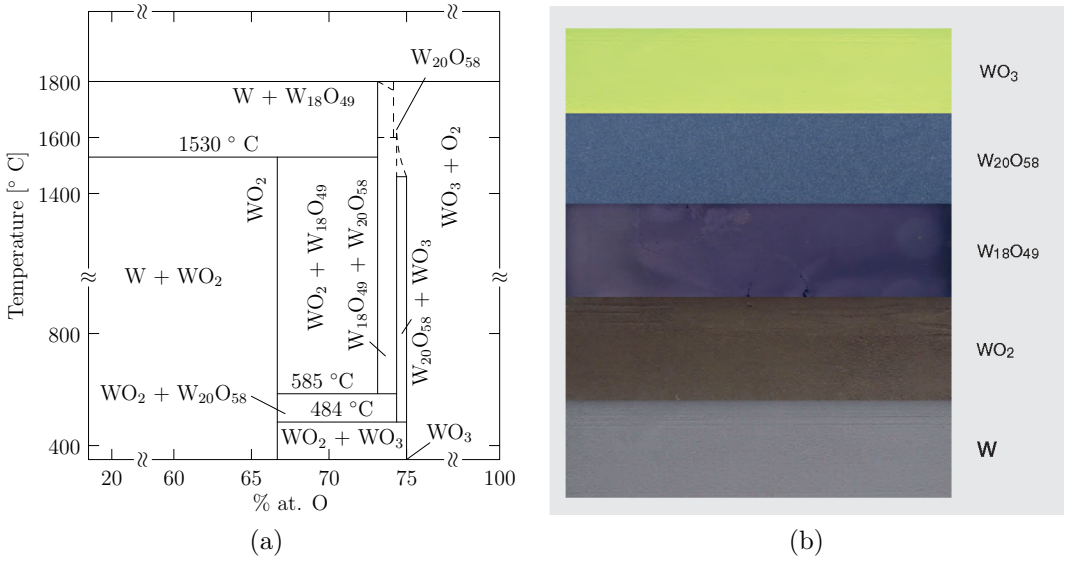

(a) (b)

Figure 1: (a) W-O phase diagram, adapted from ref. [27]. (b) Colors of the tungsten oxides: yellow WO_3, blue $WO_{2.9}$, violet $WO_{2.72}$, chocolate-brown for WO_2, and gray for the W metal. From ref. [28].

in Fig. 1a, $WO_{2.9}$ only exists above 484°C, while $WO_{2.72}$ is expected to appear only above 585°C. WO_3 and WO_2 exist as equilibrium phases in the entire temperature range. All these oxides appear as strong line compounds in the phase diagram, suggesting that the should form with near perfect stoichiometry. It is worth remarking that, despite their importance, the redox reactions above are not rate-limiting, as they are governed by reaction rates that occur over times that are orders of magnitude shorter than diffusive timescales. We demonstrate this quantitatively in Appendix A.2.

Comment 1

2.2. Diffusion kinetics

The model starts with the adsorption of oxygen radicals at the surface of the material. Adsorption is a thermally activated process that sets the rate of oxygen atom ingress in the solid:

$$\dot{c}_0 = c_0 \nu_{\text{ads}} = c_0 \nu^0_{\text{ads}} \exp\left(-\frac{E_{\text{ads}}}{kT}\right) \tag{4}$$

where c_0 is the concentration of oxygen radicals in solution on the environment side, ν^0_{ads} is an oxygen pick-up rate, E_{ads} is the adsorption activation energy, k is Boltzmann's constant, and T the absolute temperature. The value of c_0 is environment-dependent, but as a reference the oxygen concentration in air under standard ambient conditions is 5.64×10^{24} m^{-3} [29]. The activation barrier for adsorption depends on the structure of the surface, and ranges between 0.1 and 1.0 eV [30–32]. For lack of better data, here we take $\nu^0_{\text{ads}} = 10^{12}$ Hz and $E_{\text{ads}} = 1.0$ eV. Note that the model can be solved using both $\dot{c}_0$ or c_0 as boundary conditions on the environmental side.

The model of oxide growth can then be formulated by considering the motion of four interfaces, each characterized by its own evolution equation. Together, the motions of these interfaces determinate the rate of oxidation of the underlying metal substrate. Note that this means that the oxide grows into the metal, which is the correct physical assumption due to mass conservation. As well, here we ignore the relative volumetric expansion of the oxide layers relative to the initial metal phase. The evolution equations can be written assuming a sharp-interface model (known as a Stefan model) in one dimension:

$$\dot{s}_i(x) = \frac{\Delta J_i|_{s_i}}{n_i \rho_{\text{W}}} \tag{5}$$

where the subindex i refers to a specific interface, x is the depth coordinate, $\Delta J_i|_{s_i}$ is the net flux of (free) oxygen exiting the interface towards the interior, n_i is the O-to-W atomic ratio, and ρ_{W} is the atomic density of tungsten. The above equation describes the rate of advance of a specific interface on the basis of the oxygen flux differential on both sides of the interface. In essence, an interface must move to maintain mass continuity dynamically. The full derivation of eq. 5 is contained in Appendix B. To determine $\Delta J_i|_{s_i}$, one must solve a diffusion equation in each oxide sublayer to first determine the free oxygen concentration profile and then obtain the

flux using Fick's first law:

$$\Delta J_i|_{s_i} = J_i|_{s_i+} - J_i|_{s_i-} = D_i \frac{\partial c}{\partial x}\Big|_{s_i+} - D_{i-1} \frac{\partial c}{\partial x}\Big|_{s_i-} \tag{6}$$

$$\frac{\partial c}{\partial t} = D_i \frac{\partial^2 c}{\partial x^2} \tag{7}$$

Equation 7 is subjected to two concentration boundary conditions, one for each interface bounding each oxide sublayer. At the inner edge of the layer (i.e., at $x = s_i$), $c = 0$ always. At the outer edge of the layer ($x = s_{i-1}$), $c = \rho_{\mathrm{W}} (n_{i-1} - n_i)$. The exceptions to this are the outermost and innermost layers (which are both fixed, i.e., $\dot{s}_0 = \dot{s}_5 = 0$), where $c = c_0$ and $J_5 = 0$, respectively. The specific values for each sublayer are given in Table 1.

Table 1: Details for the formulation of the Stefan model of multilayer interface evolution.

Layer	Compound	n	Outer interface	Inner interface	Outer boundary condition [ρ_{W}]	Inner boundary condition [ρ_{W}]
1	WO_3	3.0	s_0	s_1	$c = c_0$	$c = 0$
2	$WO_{2.90}$	2.90	s_1	s_2	$c = 0.1$	$c = 0$
3	$WO_{2.72}$	2.72	s_2	s_3	$c = 0.18$	$c = 0$
4	WO_2	2.0	s_3	s_4	$c = 0.72$	$c = 0$
5	W-O metal	-	s_4	s_5	$c = 2.0$	$J = 0$

2.3. Multilayer structure

Note that here we are assuming that all the oxygen above the stoichiometric concentration in each layer is insoluble in that layer, while according to the phase diagram some of it starts to precipitate as the next phase richer in oxygen. However, here we treat this as having a minor effect on the kinetics. As well, a delayed formation of a WO_x phase can take place even when the oxygen concentration is lower than $x\rho_{\mathrm{W}}$. In that case, as eq. 4 indicates, building up the oxygen concentration up to the required value for each stoichiometric oxide phase to form, takes an amount of

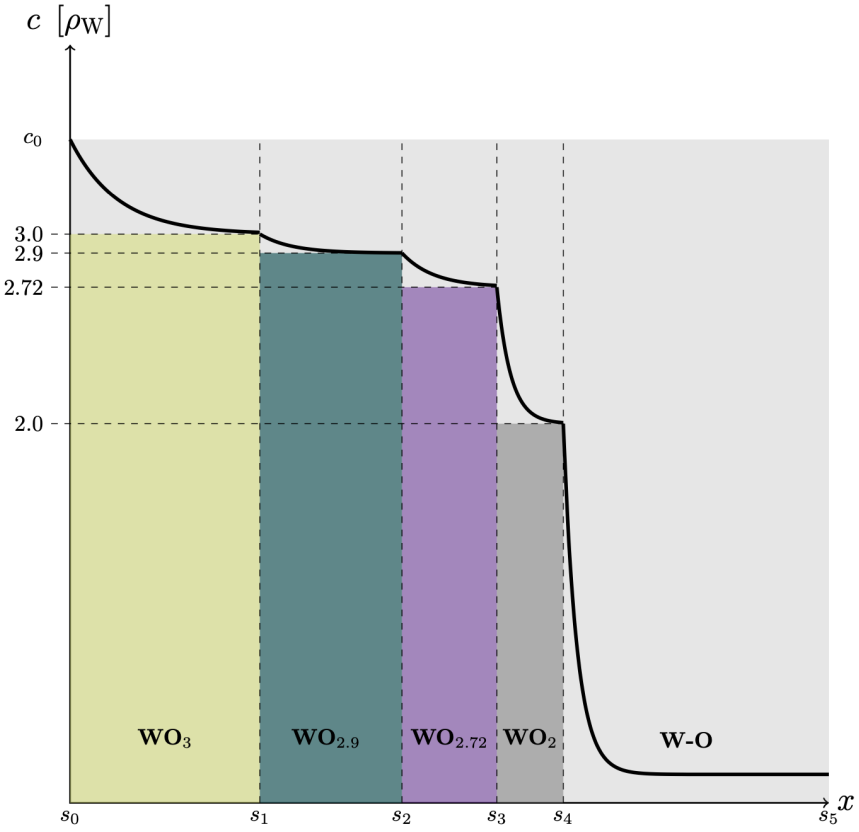

Figure 2: Schematic representation of the multilayer system in steady state. The absorbed oxygen is partitioned into 'chemical' oxygen, which is immobilized in the oxide structures themselves, and 'free' oxygen, which diffuses through each layer and is represented by a concentration profile shown as a thick black line. Note that the width of each layer is arbitrary in the figure.

time given by $\Delta t = x/\dot{c}_0$. The assumption made in this work is that this time does not compute towards the total oxide layer formation time. The equations to be solved for each layer, with the appropriate numerical notation and boundary conditions to be used are given below. To indicate the boundary conditions on the right-hand side of a given interface i (with respect to the frame of reference on Figure 2), the suffix 's_i+' ('s_i-' to refer to the left side).

Layer 1:

Material	WO_3
Governing equations	$\dot{s}_1(x) = \frac{\Delta J_1\|_{s_1}}{3.0\rho_W}$ $\Delta J_1\|_{s_1} = D_2 \frac{\partial c}{\partial x}\Big\|_{s_1+} - D_1 \frac{\partial c}{\partial x}\Big\|_{s_1-}$ $\frac{\partial c}{\partial t} = D_1 \frac{\partial^2 c}{\partial x^2}$
Boundary conditions	$c(0) = c_0 - 3\rho_W,\ c(s_1) = 0$ (as well : $\dot{c}(0) = \dot{c}_0$)

Layer 2:

Material	$WO_{2.9}$
Governing equations	$\dot{s}_2(x) = \frac{\Delta J_2\|_{s_2}}{2.9\rho_W}$ $\Delta J_2\|_{s_2} = D_3 \frac{\partial c}{\partial x}\Big\|_{s_2+} - D_2 \frac{\partial c}{\partial x}\Big\|_{s_2-}$ $\frac{\partial c}{\partial t} = D_2 \frac{\partial^2 c}{\partial x^2}$
Boundary conditions	$c(s_1) = 0.1\rho_W,\ c(s_2) = 0$

Layer 3:

Material	$WO_{2.72}$
Governing equations	$\dot{s}_3(x) = \frac{\Delta J_3\|_{s_2}}{2.72\rho_W}$ $\Delta J_3\|_{s_3} = D_4 \frac{\partial c}{\partial x}\Big\|_{s_3+} - D_3 \frac{\partial c}{\partial x}\Big\|_{s_3-}$ $\frac{\partial c}{\partial t} = D_3 \frac{\partial^2 c}{\partial x^2}$
Boundary conditions	$c(s_2) = 0.18\rho_W,\ c(s_3) = 0$

Layer 4:

Material	WO_2
Governing equations	$\dot{s}_4(x) = \frac{\Delta J_4\|_{s3}}{2.0\rho_W}$ $\Delta J_4\|_{s_4} = D_5 \frac{\partial c}{\partial x}\Big\|_{s_4+} - D_4 \frac{\partial c}{\partial x}\Big\|_{s_4-}$ $\frac{\partial c}{\partial t} = D_4 \frac{\partial^2 c}{\partial x^2}$
Boundary conditions	$c(s_3) = 0.72\rho_W,\ c(s_4) = 0$

Layer 5:

Material	W-O (metal)
Governing equations	$\frac{\partial c}{\partial t} = D_5 \frac{\partial^2 c}{\partial x^2}$
Boundary conditions	$c(s_4) = 2.0\rho_W,\ J(s_5) = 0$

The above model builds on similar approaches devised to study diffusion in multilaminates [33]. When a given layer cracks, a modification to the above formulation must be adopted. When a layer i bounded by oxygen concentrations of c_{i-1} and c_i fragments after it reaches a critical width, w_i^*, it opens up percolation pathways that equalize the free oxygen concentration across it [34], i.e., $c_{i-1} = c_i$. When such a situation arises, the layer in question stops growing and simply acts as an oxygen bridge between its two adjacent layers. During the simulations that will be presented below, a provision is introduced in the model to switch to this mode of oxygen transport once w_i^* is reached.

Comment 4

2.4. Discretized multilayer equations

Here we adopt a first-order finite difference scheme to solve the diffusion equations (Fick's 1st and 2nd laws) given in the previous sections. A one-dimensional central

finite difference approach results in the following discretized form:

$$c_i^{n+1} = c_i^n + \delta t D \left(\frac{c_{i+1}^n - 2c_i^n + c_{i-1}^n}{\delta x^2} \right) \tag{8}$$

$$J_i^n = -D \frac{c_{i+1}^n - c_{i-1}^n}{2\delta x} \approx -D \frac{c_i^n - c_{i-1}^n}{\delta x} \tag{9}$$

where δt and δx are the time and space increments, and the subindices n and i refer to temporal and spatial steps. Both equations above are subjected to the Neumann stability condition $\delta t < \delta x^2/D$.

Application of the boundary conditions leads to:

$$c_i^0 = 0, \; c_0^n = c_0, \; c_{s_5}^n = c_{s_5 - \delta x}^n$$

While the total oxygen concentration (stoichiometric plus free) is continuous at each interface, each diffusion equation in each layer is solved only for the free oxygen concentration. This results in jumps in the concentration depending on whether one looks at the interface from the left or from the right in Fig. 2. With the coordinate x arriving at each interface, one has:

$$c_{s_1}^n = c_{s_2}^n = c_{s_3}^n = c_{s_4}^n = 0$$

and with x leaving each interface:

$$c_{s_1}^n = 0.10, \; c_{s_2}^n = 0.18, \; c_{s_3}^n = 0.72, \; c_{s_4}^n = 2.00$$

all in units of ρ_{W}.

2.5. Material parameters and DFT calculations

The above model is fully defined when the external parameters, T and c_0, and the material properties, ρ_{W} and the diffusivities, are specified. Here, T and c_0 are prescribed, and the value of ρ_{W} is known. That leaves the diffusivities D_i $(i = 1, 5)$ as the remaining material constants to determine.

The general expression for the diffusion coefficient is the standard Arrhenius form:

$$D(T) = D_0 \exp\left(-\frac{E_a}{kT} \right) \tag{10}$$

where D_0 is the diffusion pre-factor and E_a is the activation energy. That means that five separate pre-factors and five activation energies must be determined for

each oxide layer. In all cases, TEM experiments have revealed that the oxide always grows into the tungsten metallic matrix, confirming that oxide growth is controlled by oxygen anion diffusion from the environment side inwards [35].

In any case, the first thing to ascertain is whether oxygen is transported by a vacancy mechanism (through exchanges with empty oxygen sublattice sites) or as interstitial atoms in an otherwise fully-occupied lattice. On first inspection of Fig. 1a, the line compound structure of all the oxide sublayers considered here (in Fig. 2) suggests that oxygen atoms will diffuse as free interstitials in all cases. However, there is sufficient consensus about the abundance of oxygen vacancies, both thermal and chemical (i.e., due to natural stoichiometric deviations) in all oxide phases [36–39], and so here we assume going forward that all oxygen transport within the oxide laters takes place via a vacancy mechanism. Next, we select oxygen diffusion properties for each layer shown in Sec. 2.3, either from literature sources or –if unavailable– by carrying out DFT calculations using the methodology described in Appendix C.1.

2.5.1. WO_3 layer Sikka and Rosa [17] studied oxidation of pure W in the 568-908°C interval and measured an oxygen diffusivity of $D(T) = 6.83 \times 10^{-6} \exp(-1.3/kT)$ [$\mathrm{cm^2 \cdot s^{-1}}$]. Such experiments are conducted under the assumption that tungsten trioxide is under some slight deviation, represented by x (not to be confused with the spatial coordinate), from stoichiometry. i.e., in WO_{3-x}. The measured activation energy of 1.3 eV is indeed suggestive of a vacancy mechanism if one takes the activation energy as being the sum of the oxygen vacancy formation and migration energies. DFT calculations of oxygen vacancy formation energies consistently yield values of ≈1.5 eV [37, 40], while for the migration energy alone, energies between 0.4 and 0.9 eV are obtained [40, 41].

With this, we take the values measured by Sikka and Rosa [17] for $D_1(T)$.

2.5.2. WO_2 layer In contrast to WO_3, no data are available for oxygen diffusion in WO_2 and we proceed to calculate O diffusivity in layer 4. Here too, a vacancy mechanism is assumed. The starting point for the calculations is an expanded expression for the diffusivity:

$$D_4(T) = z c_{\mathrm{V}}(T) \ell^2 \nu(T) \tag{11}$$

where z is a geometric factor, ℓ is the jump distance,

$$c_{\mathrm{V}}(T) = \exp\left(-\frac{E_f^{\mathrm{V}}}{kT}\right)$$

is the thermal vacancy concentration (E_f^{V} is the oxygen vacancy formation energy), and

$$\nu(T) = \nu_0 \exp\left(-\frac{E_m^{\mathrm{V}}}{kT}\right)$$

is the jump frequency with E_m^{V} the oxygen vacancy migration energy. Equations 10 and 11 imply that $D_0 = z\ell^2\nu_0$ and $E_a = E_m^{\mathrm{V}} + E_f^{\mathrm{V}}$. The factor z, which includes the number of jump sites n_p and the dimension of diffusion d, is $n_p/2d = 5/3$, and the jump distance ℓ is 2.76 Å for the oxygen sub-lattice in WO_2 [42, 43]. In this work, E_f^{V}, E_m^{V}, and ν_0 were obtained using DFT calculations as reported in Appendix C.2. The final expression for $D_4(T)$ is given in eq. C.6.

2.6. $WO_{2.9}$ and $WO_{2.72}$ layers

No data whatsoever exist for the diffusivity of oxygen in the $WO_{2.9}$ and $WO_{2.72}$ layers. In their analysis of oxidation kinetics data, Nagy and Humphry-Baker identified three bands of oxygen partial pressure, low (0.1 atm), medium (0.2 atm), and high (3.4∼13.6 atm). They extracted effective activation energies of 1.22, 1.40, and 1.94 eV for each one [26]. By mapping O partial pressures to oxygen/metal ratio, these can loosely be ascribed to diffusion in $WO_{2.72}$, $WO_{2.9}$, and WO_3, respectively. Indeed, these energies are not inconsistent with the values of 1.3 and 1.5 eV measured and calculated for oxygen diffusion in WO_3 [17, 37]. We thus select 1.22 and 1.40 eV as the activation energies for $WO_{2.72}$, $WO_{2.9}$. In terms of the prefactor, for lack of a more suitable option, here we take that in D_1 to be the same in D_2 and D_3.

2.6.1. Metallic W The solubility of oxygen in W is very low [15] and O atoms are found primarily in interstitial positions. Specifically, interstitial oxygen is seen to diffuse in the W lattice throughout tetrahedral positions with a migration energy of 0.15 eV [44]. The diffusion pre-factor has been obtained by Alkhamees *et al* [45] to be 7.6×10^{-8} $\mathrm{m^2{\cdot}s^{-1}}$, i.e.:

$$D_5(T) = 7.6 \times 10^{-8} \exp\left(-\frac{0.15}{kT}\right) \quad [\mathrm{m^2 \cdot s^{-1}}] \tag{12}$$

Table 2 lists all the diffusivities used in the multilayer model.

Table 2: Compilation of diffusivity parameters used in the multilayer tracking model developed in this work.

Diffusivity	Material	D_0 [$m^2 \cdot s^{-1}$]	E_m^V [eV]
D_1	WO_3	6.8×10^{-6}	1.3
D_2	$WO_{2.9}$		1.40
D_3	$WO_{2.72}$		1.22
D_4	WO_2	3.1×10^{-5}	1.90
D_5	W metal	7.6×10^{-8}	0.15

2.7. Critical fragmentation widths

As indicated at the end of Sec. 2.3, fragmentation of an oxide scale occurs due to the large epitaxial misfit between the metal substrate and the oxide phase. These creates residual stresses (known as Pilling-Bedworth stresses) that put the oxide under compression, building up as the layer grows. At a critical thickness threshold, which we term w^*, the layer fragments generally creating a network of cracks through which oxygen can flow unimpeded [34]. At this stage, oxygen transport ceases to be the rate limiting step in oxide layer growth, which is subsequently seen to scale linearly with time. Linear growth can also coexist with parabolic (diffusive) growth. Indeed, the presence of exponents between 0.5 and 1.0 in oxidation experiments is suggestive of the coexistence of cracked layers and protective layers [19, 26].

By its own definition, these stresses set in only between the oxide phase immediately in contact with the metallic base. As such, in a multilayer setting as the present one, one would expect only one single layer to undergo cracking at any give time. A compilation of data relating temperature, critical width w^*, and oxide phase is provided in Table A1 (Appendix A.2). These are based on measurements performed by Gulbransen and Andrew [16] and analyzed by Nagy and Humphry-Baker [26]. As the table shows, the WO_2 phase is common to all oxidation conditions, consistent with the expectation that it should be the layer immediately adjacent to

the metal substrate§ On the basis of these data, in the forthcoming simulations, we assume that in impoverished oxygen atmospheres, a WO_2 layer forms and grows up to a temperature-dependent thickness given by the listed values of w^*.

3. Results

3.1. Oxide growth simulations as a function of temperature

Next, we present results of the oxide layer growth as a function of temperature. Based on the qualitative observations by Gulbransen et al. (Table A1), where broadly three oxidation regimes were observed as a function of T, here we consider the following three temperature regions : (i) at or below 600°C (873 K), (ii) between 600 and 800°C (873 to 1073 K), and (iii) at or above 800°C. We initialize the model with the temperature value and a boundary oxygen concentration, c_0, that favors the formation of the oxide phases listed in Table A1. We set δt and δx to 1 ns and 1 nm, respectively, which are sufficiently small to always guarantee the numerical stability of the finite-difference solution procedure. In all cases, we show results for the first 30 s of evolution, when the thickness of all oxide layers involved is well below the fragmentation threshold (second column of Table A1). As such, the results presented below correspond to the regime when the oxide maintains its protective structure, which can thus be assumed until its thickness reaches the critical width at each temperature.

Comment 3

We give the results in each case as a pair of plots, one showing the depth profiles of all the sublayers involved color-coded by the time instant for which they are displayed, and the other showing the position of the different interfaces as a function of time. c is always given in units of ρ_W. The depth profiles are always color-coded by the scale used in Fig. 1b to facilitate the identification of each oxide type.

3.1.1. Kinetic model simulations at 600°C The results at this temperature are shown in Figure 3. As indicated in Table A1, only $WO_{2.72}$ and WO_2 form at this temperature. Figure 3a reveals a very thin WO_2 layer behind $WO_{2.72}$, also captured

§ However, care should exercised in utilizing these data, as they were obtained in depleted oxygen conditions where WO_2 and $WO_{2.72}$ phases would be favored.

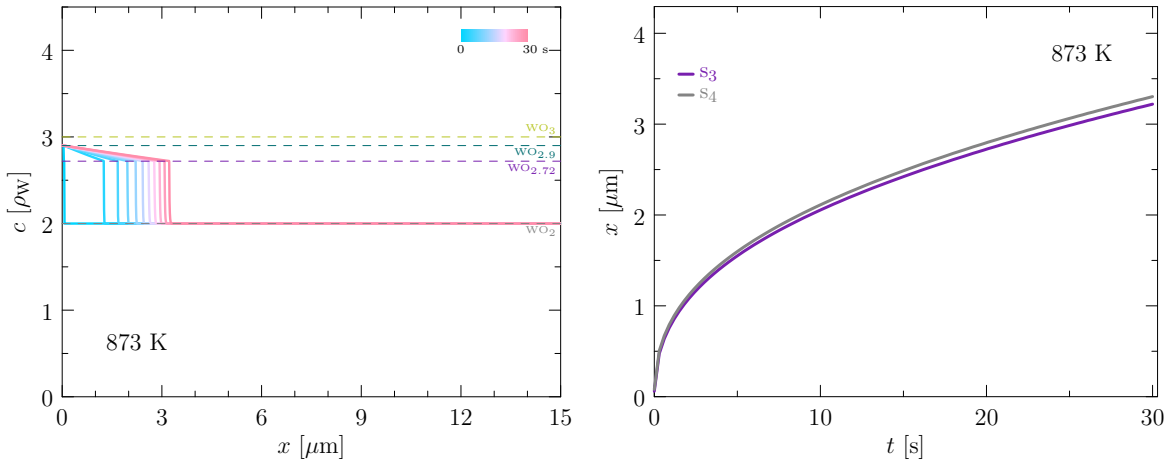

Figure 3: (a) Depth-time profiles of the oxide layer structure at 873 K. (b) Time evolution of the $WO_{2.72}/WO_2$ (s_3) and WO_2/metal (s_4) interfaces during the first 30 s of exposure.

in Fig. 3a. A power law fit to the s_4-t graph yields $s_4(t) = 3.747t^{0.407}$, indicating a substantial deviation from pure parabolic growth law.

3.1.2. Kinetic model simulations at $600 < T < 800°C$ The slow growth of the WO_2 layer carries over to the simulations at 650 and 700°C (923 and 973 K). At 650°C, however, all oxide sublayers are present, Figs. 4a and 4b, with WO_3 also displaying slow growth kinetics. At 700°C, Figs. 4c and 4d, the evolution is qualitative similar to that at 600°C given in the previous subsection. In this case, the growth law exponents at 650 and 700°C are 0.41 and 0.44.

3.1.3. Kinetic model simulations at and above 800°C Figure 5 shows the corresponding graphs at 800 and 1000°C. At these temperatures, again according to the observed phases in the experiments listed in Table A1, only the WO_2 phase forms. Interestingly, at 800°C the growth kinetics is quite slow, with the power law fit being $s_4(t) = 1.852t^{0.454}$ (in microns). By contrast, at 1000°C the temperature is sufficiently high to overcome the diffusion barrier of oxygen in WO_2, giving rise to faster kinetics compared to the previous scenarios. As such, the fitted expression

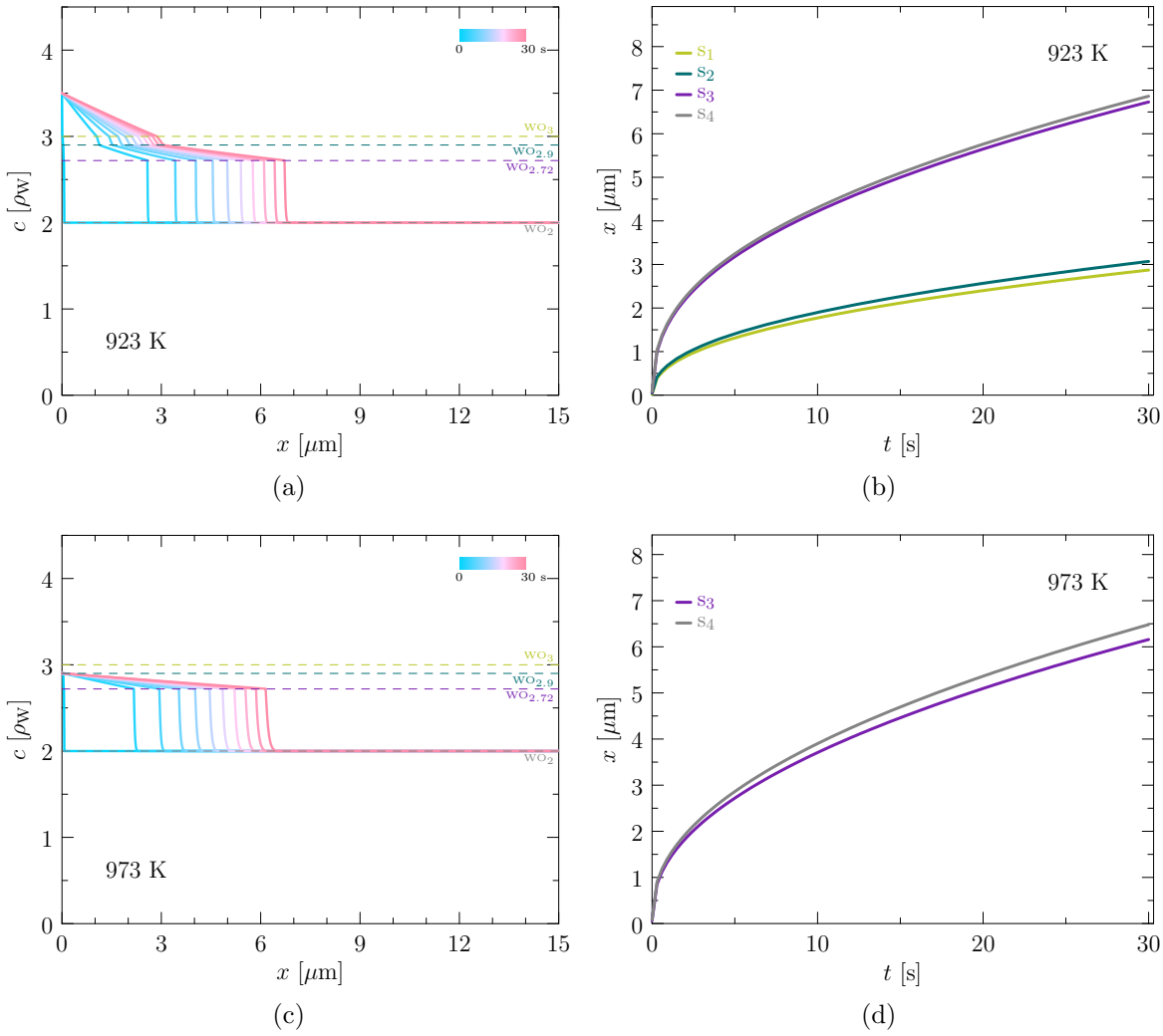

Figure 4: Depth-time profiles of the oxide layer structure at 923 (a) and 973 K (c). Corresponding time evolution of the different oxide interfaces interfaces during the first 3 s of exposure, (b) and (d).

in this case is $s_4(t) = 7.812t^{0.490}$. As revealed by the value of the power exponents, having one layer only forming part of the oxide significantly approximates the kinetics to the pure parabolic case.

All the fitting coefficients are compiled for each temperature in Table 3. It is worth mentioning that the power law exponents obtained here are similar to those

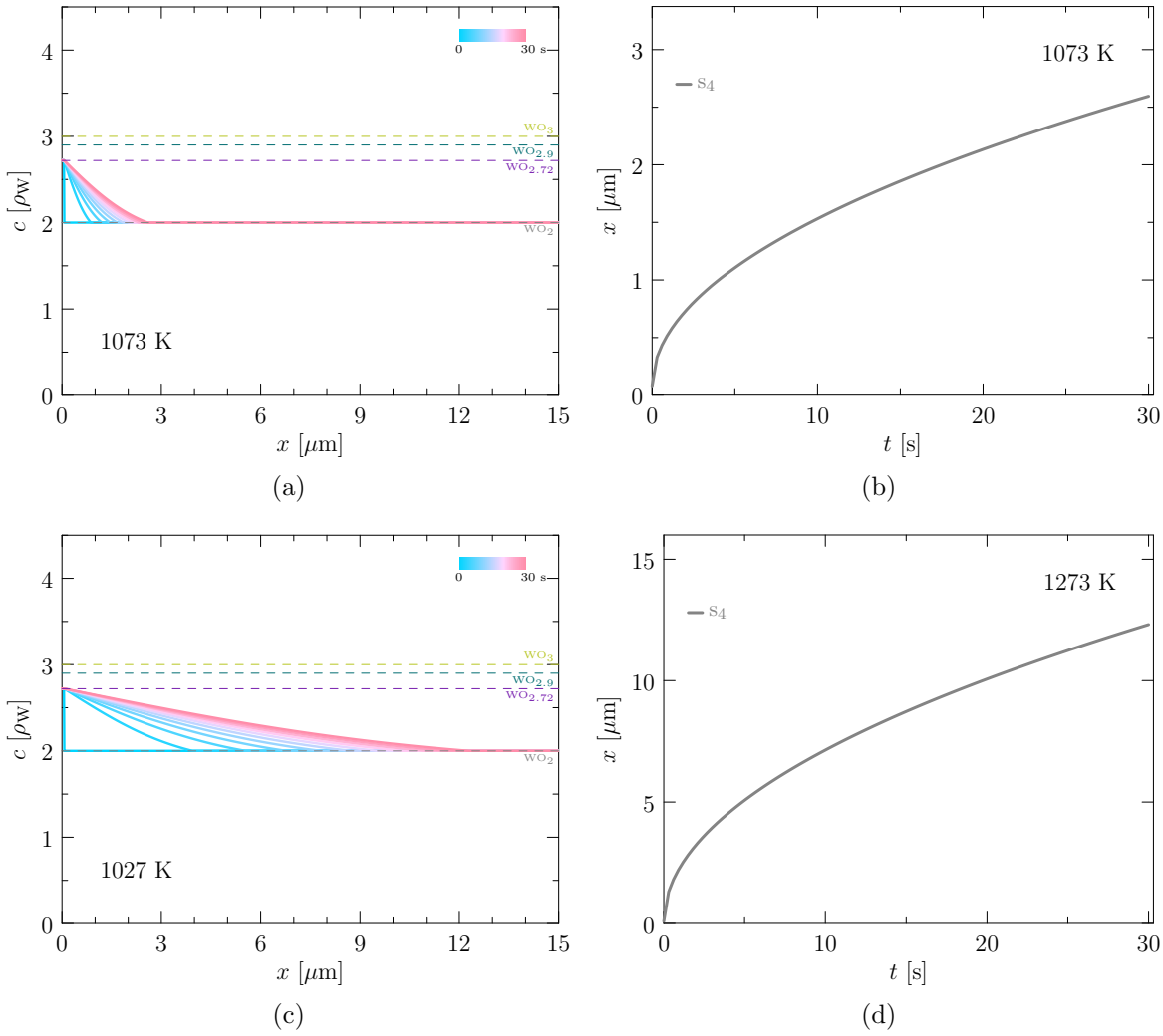

Figure 5: Depth-time profiles of the oxide layer structure at 1073 (a) and 1273 K (c). Corresponding time evolution of the different oxide interfaces interfaces during the first 3 s of exposure, (b) and (d).

measured in SMART W-based alloys [10, 46].

Table 3: Power law fitting coefficients $s_i(t) = at^b$ for all the temperatures considered in this work. Sublayer thickness given in units of microns.

T [K]	number of sublayers	a	b	k_p [mg^2 cm^{-4} min^{-1}]
873	2	3.747	0.407	4.28
923	4	7.930	0.413	20.31
973	2	6.435	0.441	16.69
1073	1	1.852	0.454	3.85
1273	1	7.812	0.490	34.20

4. Discussion

4.1. Main feature of the numerical model

The model presented here is formulated as a Stefan interface tracking approach where different oxide/oxide and oxide/metal interfaces evolve in time driven by discontinuities in oxygen fluxes across each one of them. These fluxes emerge in each oxide sublayer from the diffusion of free oxygen (i.e., not chemically immobilized) as a function of temperature. As such, it is crucial to have accurate oxygen diffusivities for the different oxide layers. These can be inferred from mass gain experiments, by assuming parabolic growth laws governed by pure diffusion. Unfortunately, most experimental works do not discriminate among the different oxide subphases, which has prompted the use of computational techniques to calculate the diffusivity in specific WO compounds [47, 48]. Even then, the computational data is scarce and does not address many of the gaps in our understanding of oxygen diffusion in tungsten oxide. For example, it is not clear whether oxygen diffusion primarily takes place by an interstitial or a vacancy mechanism in each of the different oxide phases. Here, we have applied electronic structure calculations to quantify the migration parameters of oxygen atoms in WO_2 by a vacancy mechanism, which was lacking in the literature.

From this point of view, this work is a first attempt at embedding the thermodynamic and kinetic complexity of tungsten oxide growth into a comprehensive mesoscale kinetic model that captures the more important features of the oxidation process. Below we provide further discussion about how the model

has been designed, implemented, and validated.

4.2. Physical model validity

In this work, the simulated oxide structures are inspired by empirical observations of the outermost oxide layer during environmental exposure of pure W [16,17,19,49] (see Appendix A.2). Of note is the apparent absence of tungsten trioxide in oxidized samples. Indeed, WO_3 is not customarily seen to form as a standalone layer in the majority of experimental works scrutinized in this work. Instead, WO_3 forms only after lower order oxides have grown and cracked, allowing for fast oxygen transport pathways that stimulate the formation of the trioxide. For example, in a recent work Cifuentes et al. [19] note that, at 600°C, the oxidation was initially controlled by the development of a continuous $WO_{2.72}$ layer, which grows until it starts cracking leading to linear kinetics. At 700 and 800°, after cracking of the $WO_{2.72}$ layer, $WO_{2.92}$ is progressively seen to form, eventually turning into WO_3 in the course of the oxidation. Other times, $WO_{2.92}$ volatilization after cracking exposes tungsten to the exposed surface, leading to the formation of a yellow external WO_3 layer [19]. This evidence points to a mechanism of formation of WO_3 by which its formation takes place only after the $WO_{2.72}$ (and WO_2, discussed further below) layer has fragmented and lost its protective abilities.

The lack of stated observation of WO_2 in many of these experiments may be due to its intrinsic small thickness. Indeed, our calculations suggest that oxygen transport through tungsten dioxide is slow (mostly owing to a migration energy of almost 2.0 eV, Table 2), making WO_2 a true protective layer. Only above 1000°C is WO_2 seen to form at high rates, although at such temperatures all oxide layers start becoming structurally unstable due to sublimation. On this point, it must be noted that sublimation is not a feature of the present model, although studies have consistently shown that it becomes the dominant effect at high temperatures [50,51]. Comment 5

Based on this presumed behavior, our interpretation of the kinetics of oxide growth is that: (i) the free oxygen concentration under nominal conditions is generally never sufficiently high to form WO_3 directly; (ii) the most common oxide sublayers are $WO_{2.72}$ and WO_2; (iii) these layers will grow in a protective fashion until a critical thickness is reached, at which point cracking occurs and the oxygen-rich phases $WO_{2.92}$ and WO_3 begin to form; (iv) whenever multiple oxide sublayers form in succession, deviations from the standard parabolic growth law are clearly

seen. In our case, fracture and fragmentation is not a part of the current model, and we control the formation of the different oxides simply by regulating the amount of available oxygen, c_0, on the environment side of the exposed metal. c_0 is in fact the only parameter of our model that is 'adjusted' to reproduce certain observations.

4.3. Comparison to experimental measurements

A useful exercise is to compare the growth kinetics simulated in this work to available experimental data. As is customary in most works, oxide scale growth is measured in terms of tungsten mass gain assuming parabolic growth. Consequently, the mass gain constant is obtained from first to the data expressed linearly in time.

$$(\Delta m)^2 = [(n\rho_{\mathrm{W}})s_4(t)]^2 = k_p t$$

where Δm is the mass gain, $n\rho_{\mathrm{W}}$ is the amount of oxygen gained when a WO_n oxide forms (expressed as a mass density), and k_p is the parabolic kinetic constant. Next, we fit all the sublayer evolutions shown in Figs. 3-5 to ideal parabolic growth expressions and plot the simulated values of k_p in Figure 6 along with a set of experimental measurements. The numerical values of k_p extracted from the simulations are also given in Table 3.

The results show that, while the simulated values generally overestimate the experimental measurements, they lie within the broader range of the data at some temperatures. However, it is worth noting that the experimental results are not all representative of the same conditions. Indeed, broadly speaking, they can be divided into two categories: short and long exposures to the oxidizing medium. For example, in the experiments by Sikka et al. [17], the samples were exposed only for several hundred seconds, while in all the other cases [16, 19, 49], they were exposed to oxygen for several hours. Given the slow diffusivity of oxygen across most of the oxide phases, hundreds of seconds may not be a sufficiently long time to reach visible thickness. Using one micron as the minimum observable oxide thickness (reasonable based on the data in Table A1), the diffusive time scales for oxygen transport in the outer layers (WO_3, $\mathrm{WO}_{2.9}$, and $\mathrm{WO}_{2.72}$), and in WO_2 at 850 K are respectively 7.5 s and 1.7 h, approximately (estimated using the diffusivities reported in Table 2). Therefore, within the short timescales simulated here (≈30 s) and those in the experiments by Sikka et al. (≈200 s), the oxide layers may not have fully reached a steady growth rate. The exact diffusive timescale will vary depending on the temperature and there-

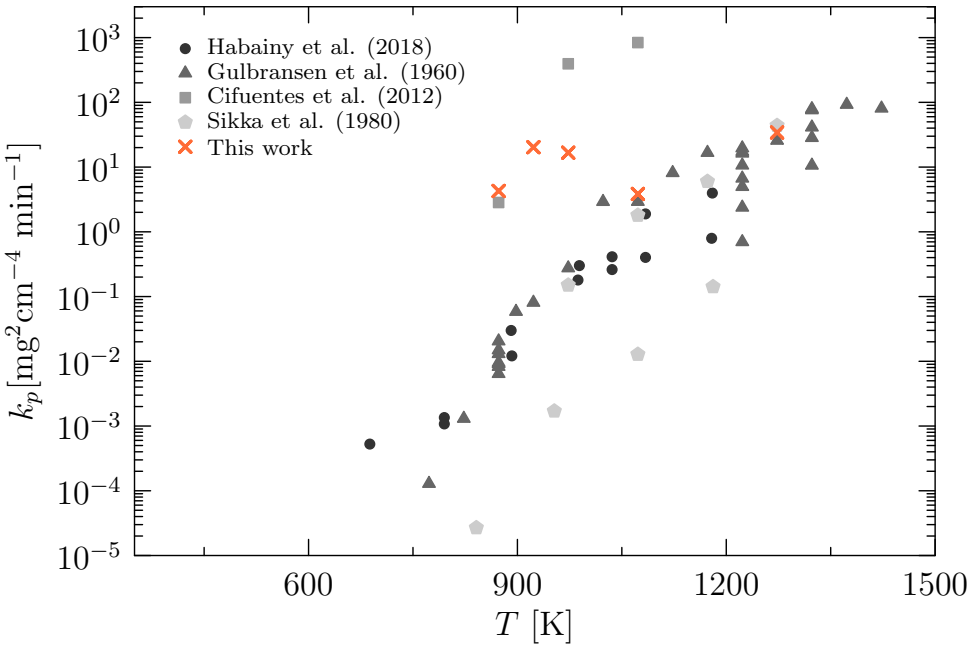

Figure 6: Parabolic growth constant as a function of temperature from a set of experimental data and as obtained in this work. Experimental data from Habainy et al. (2018) [49], Gulbransen et al. (1960) [16], Cifuentes et al. (2012) [19], and Sikka et al. (1980) [17].

fore not all the experimental data may correspond to the same kinetic state. In any case, given the figurative 'distance' between how the model was developed and how experiments are performed, we consider these differences reasonable.

Comment 6

5. Conclusions

We finalize with our main conclusions:

(i) We have developed an interface-tracking model to simulate the kinetic evolution of multiple tungsten oxide layers. The model is consistent with the observed equilibrium oxide phases in the W-O phase diagram, and uses the diffusivities as the only material constants. The model is solved in space and time by adopting a finite-difference approach in one dimension with length and time increments of 1 nm and 1 ns, respectively.

(ii) We have parameterized the model using diffusivities both from experimental and computational sources. Due to the lack of available information for the diffusivity of oxygen in WO_2, we have carried out a series of DFT calculations to calculate the migration energy and diffusion pre-factor of oxygen in WO_2 by a vacancy mechanism.

(iii) We consider only the protective growth stage of the oxide, before the critical fragmentation thickness is reached and the oxide layers begin to fail. This stage is believed to be captured by so-called 'parabolic' growth behavior, while after cracking growth is generally characterized by linear time kinetics.

(iv) The time evolution of the oxide scale matches parabolic growth only at high temperatures and when only one oxide sublayer is involved. Whenever multiple layers are at play, measurable deviations from parabolic growth can be appreciated.

(v) The calculated values for the mass gain proportionality constant are in reasonable agreement with experimental measurements from several independent data sources. This adds validity to the model, particularly since the model is not fitted to experimental results a posteriori.

Acknowledgments

Acknowledgements SH and JM acknowledge support from the US Department of Energy's Office of Fusion Energy Sciences, project DE-SC0012774. MG acknowledges funding from the EPSRC Energy Programme [grant number EP/W006839/1].

Data Availability

The raw data and modeling software required to reproduce these results can be provided by the authors upon reasonable request.

References

[1] J. C. Scully, Fundamentals of corrosion, Pergamon Press Inc., Elmsford, NY, 1975.

[2] N. North, I. D. MacLeod, C. Pearson, Corrosion of metals, Butterworth-Heinemann, 1987.

[3] D. J. Young, High temperature oxidation and corrosion of metals, Vol. 1, Elsevier, 2008.

[4] K. Tomabechi, J. Gilleland, Y. A. Sokolov, R. Toschi, I. Team, et al., Iter conceptual design, Nuclear Fusion 31 (6) (1991) 1135.

[5] R. Aymar, P. Barabaschi, Y. Shimomura, The iter design, Plasma physics and controlled fusion 44 (5) (2002) 519.

[6] G. Federici, R. Kemp, D. Ward, C. Bachmann, T. Franke, S. Gonzalez, C. Lowry, M. Gadomska, J. Harman, B. Meszaros, et al., Overview of eu demo design and r&d activities, Fusion Engineering and Design 89 (7-8) (2014) 882–889.

[7] G. Smolik, S. Piet, R. Neilson Jr, Predictions of radioactive tungsten release for hypothetical iter accidents, Fusion Technology 19 (3P2B) (1991) 1398–1402.

[8] M. Rieth, S. L. Dudarev, S. G. De Vicente, J. Aktaa, T. Ahlgren, S. Antusch, D. Armstrong, M. Balden, N. Baluc, M.-F. Barthe, et al., Recent progress in research on tungsten materials for nuclear fusion applications in europe, Journal of Nuclear Materials 432 (1-3) (2013) 482–500.

[9] F. Klein, T. Wegener, A. Litnovsky, M. Rasinski, X. Tan, J. Gonzalez-Julian, J. Schmitz, M. Bram, J. Coenen, C. Linsmeier, Oxidation resistance of bulk plasma-facing tungsten alloys, Nuclear materials and energy 15 (2018) 226–231.

[10] A. Litnovsky, T. Wegener, F. Klein, C. Linsmeier, M. Rasinski, A. Kreter, X. Tan, J. Schmitz, J. Coenen, Y. Mao, et al., New oxidation-resistant tungsten alloys for use in the nuclear fusion reactors, Physica Scripta 2017 (T170) (2017) 014012.

[11] A. Calvo, K. Schlueter, E. Tejado, G. Pintsuk, N. Ordás, I. Iturriza, R. Neu, J. Pastor, C. García-Rosales, Self-passivating tungsten alloys of the system w-cr-y for high temperature applications, International Journal of Refractory Metals and Hard Materials 73 (2018) 29–37.

[12] T. Fu, K. Cui, Y. Zhang, J. Wang, F. Shen, L. Yu, J. Qie, et al., Oxidation protection of tungsten alloys for nuclear fusion applications: A comprehensive review, Journal of Alloys and Compounds 884 (2021) 161057.

[13] D. Maisonnier, I. Cook, S. Pierre, B. Lorenzo, G. Luciano, N. Prachai, P. Aldo, P. Team, et al., Demo and fusion power plant conceptual studies in europe, Fusion Engineering and Design 81 (8-14) (2006) 1123–1130.

[14] L. EL-GUEBALY, C. Latgé, F. Dacquait, A. AERTS, A. BARON-WIECHEC, A. BOJANOWSKA, I. CRISTESCU, U. FISCHER, S. FUKADA, M. GARCIA, et al., Overview of coolant characteristics under irradiation: Radiation-chemistry, radiolysis, activation, and their consequences on operation, maintenance, and decommissioning, IAEA TECDOC SERIES (2020) 26.

[15] E. Lassner, W.-D. Schubert, Important aspects of tungsten chemistry, in: Tungsten, Springer, 1999, pp. 85–132.

[16] E. Gulbransen, K. Andrew, Kinetics of the oxidation of pure tungsten from 500 to 1300 c, Journal of the Electrochemical Society 107 (7) (1960) 619.

[17] V. Sikka, C. Rosa, The oxidation kinetics of tungsten and the determination of oxygen diffusion coefficient in tungsten trioxide, Corrosion Science 20 (11-12) (1980) 1201–1219.
[18] C. Nilsson, J. Habainy, Oxidation of pure tungsten in the temperature interval 400 to 900 c, Diploma work.
[19] S. C. Cifuentes, M. Monge, P. Pérez, On the oxidation mechanism of pure tungsten in the temperature range 600–800 c, Corrosion Science 57 (2012) 114–121.
[20] M. Reyes, A. Aryanfar, S. W. Baek, J. Marian, Multilayer interface tracking model of zirconium clad oxidation, Journal of Nuclear Materials 509 (2018) 550–565.
[21] T. Hirai, S. Panayotis, V. Barabash, C. Amzallag, F. Escourbiac, A. Durocher, M. Merola, J. Linke, T. Loewenhoff, G. Pintsuk, et al., Use of tungsten material for the iter divertor, Nuclear Materials and Energy 9 (2016) 616–622.
[22] T. Hirai, G. Pintsuk, J. Linke, M. Batilliot, Cracking failure study of iter-reference tungsten grade under single pulse thermal shock loads at elevated temperatures, Journal of Nuclear Materials 390 (2009) 751–754.
[23] H. Wang, Y. Xu, M. Goto, Y. Tanaka, M. Yamazaki, A. Kasahara, M. Tosa, Thermal conductivity measurement of tungsten oxide nanoscale thin films, Materials transactions 47 (8) (2006) 1894–1897.
[24] D. Maisonnier, I. Cook, S. Pierre, B. Lorenzo, B. Edgar, B. Karin, F. Robin, G. Luciano, H. Stephan, N. Claudio, et al., The european power plant conceptual study, Fusion Engineering and Design 75 (2005) 1173–1179.
[25] C. C. Mardare, A. W. Hassel, Review on the versatility of tungsten oxide coatings, physica status solidi (a) 216 (12) (2019) 1900047.
[26] D. Nagy, S. A. Humphry-Baker, An oxidation mechanism map for tungsten, Scripta Materialia 209 (2022) 114373.
[27] M. Gasik, Handbook of ferroalloys: theory and technology, Butterworth-Heinemann, 2013.
[28] M. Weil, W.-D. Schubert, The beautiful colours of tungsten oxides, International Tungsten Industry Association: London, UK (2013) 1–9.
[29] https://www.engineeringtoolbox.com/molecular-mass-air-d_679.html.
[30] R. Gomer, J. Hulm, Adsorption and diffusion of oxygen on tungsten, The Journal of Chemical Physics 27 (6) (1957) 1363–1376.
[31] J. Singleton, Adsorption of oxygen on tungsten at temperatures from 300° to 850° k, The Journal of Chemical Physics 47 (1) (1967) 73–82.
[32] R. Musket, Room-temperature adsorption of oxygen on tungsten surfaces: A review, Journal of the Less Common Metals 22 (2) (1970) 175–191.
[33] R. Ash, R. Barrer, D. Palmer, Diffusion in multiple laminates, British Journal of Applied Physics 16 (6) (1965) 873.
[34] A. Aryanfar, W. Goddard III, J. Marian, Constriction percolation model for coupled diffusion-reaction corrosion of zirconium in pwr, Corrosion Science 158 (2019) 108058.
[35] M. Togaru, R. Sainju, L. Zhang, W. Jiang, Y. Zhu, Direct observation of tungsten oxidation studied by in situ environmental tem, Materials Characterization 174 (2021) 111016.
[36] C. Lambert-Mauriat, V. Oison, Density-functional study of oxygen vacancies in monoclinic tungsten oxide, Journal of Physics: Condensed Matter 18 (31) (2006) 7361.

[37] C. Lambert-Mauriat, V. Oison, L. Saadi, K. Aguir, Ab initio study of oxygen point defects on tungsten trioxide surface, Surface science 606 (1-2) (2012) 40–45.

[38] M. Mews, L. Korte, B. Rech, Oxygen vacancies in tungsten oxide and their influence on tungsten oxide/silicon heterojunction solar cells, Solar Energy Materials and Solar Cells 158 (2016) 77–83.

[39] W. Wang, A. Janotti, C. G. Van de Walle, Role of oxygen vacancies in crystalline wo 3, Journal of Materials Chemistry C 4 (27) (2016) 6641–6648.

[40] H. M. Le, N. H. Vu, B.-T. Phan, Migrations of oxygen vacancy in tungsten oxide (wo3): A density functional theory study, Computational materials science 90 (2014) 171–176.

[41] J. Chen, Calculations of vacancy diffusivity in wo3.

[42] L. Kong, L. J. Lewis, Transition state theory of the preexponential factors for self-diffusion on cu, ag, and ni surfaces, Physical Review B 74 (7) (2006) 073412.

[43] D. Uhlmann, H. K. Bowen, W. Kingery, Introduction to ceramics (1976).

[44] Y. Zhao, L. Dezerald, J. Marian, Electronic structure calculations of oxygen atom transport energetics in the presence of screw dislocations in tungsten, Metals 9 (2) (2019) 252.

[45] A. Alkhamees, Y.-L. Liu, H.-B. Zhou, S. Jin, Y. Zhang, G.-H. Lu, First-principles investigation on dissolution and diffusion of oxygen in tungsten, Journal of Nuclear Materials 393 (3) (2009) 508–512.

[46] F. Klein, A. Litnovsky, T. Wegener, X. Tan, J. Gonzalez-Julian, M. Rasinski, J. Schmitz, C. Linsmeier, M. Bram, J. W. Coenen, Sublimation of advanced tungsten alloys under demo relevant accidental conditions, Fusion engineering and design 146 (2019) 1198–1202.

[47] H. M. Le, N. H. Vu, B.-T. Phan, Migrations of oxygen vacancy in tungsten oxide (wo3): A density functional theory study, Computational Materials Science 90 (2014) 171–176.

[48] C. Linderalv, Structural and thermodynamical properties of tungsten oxides from first-principles calculations, Master's thesis, Chalmers University of Technology (2016).

[49] J. Habainy, S. Iyengar, K. B. Surreddi, Y. Lee, Y. Dai, Formation of oxide layers on tungsten at low oxygen partial pressures, Journal of Nuclear Materials 506 (2018) 26–34.

[50] C. Tedmon, The effect of oxide volatilization on the oxidation kinetics of cr and fe-cr alloys, Journal of the electrochemical society 113 (8) (1966) 766.

[51] J. Wendel, Thermodynamics and kinetics of tungsten oxidation and tungsten oxide sublimation in the temperature interval 200–1100 c, Diploma work.

[52] A. Faudoa-Arzate, A. Arteaga-Durán, R. Saenz-Hernández, M. Botello-Zubiate, P. Realyvazquez-Guevara, J. Matutes-Aquino, Hrtem microstructural characterization of β-wo3 thin films deposited by reactive rf magnetron sputtering, Materials 10 (2) (2017) 200.

[53] H. Wriedt, The ow (oxygen-tungsten) system, Bulletin of Alloy phase diagrams 10 (4) (1989) 368–384.

[54] R. Pickering, R. Tilley, An electron microscope study of tungsten oxides in the composition range $wo_{2.9}$-$wo_{2.72}$, Journal of Solid State Chemistry 16 (3-4) (1976) 247–255.

[55] R. Tilley, The crystal chemistry of the higher tungsten oxides, The chemistry of non-sag tungsten (1995) 93–109.

[56] A. Shengelaya, F. L. Mattina, K. Conder, Unconventional transport properties of reduced

tungsten oxide wo2. 9, Condensed Matter 5 (4) (2020) 63.
[57] J. L. Sabourin, R. A. Yetter, High-temperature oxidation kinetics of tungsten-water reaction with hydrogen inhibition, Journal of Propulsion and Power 27 (5) (2011) 1088–1096.
[58] S. A. Tolba, K. M. Gameel, B. A. Ali, H. A. Almossalami, N. K. Allam, The dft+ u: Approaches, accuracy, and applications, Density Functional Calculations-Recent Progresses of Theory and Application (2018) 3–30.
[59] A. Seidl, G ? rling, a.; vogl, p.; majewski, ja; levy, m, Phys. Rev. B 53 (1996) 3764.
[60] V. I. Anisimov, F. Aryasetiawan, A. Lichtenstein, First-principles calculations of the electronic structure and spectra of strongly correlated systems: the lda+ u method, Journal of Physics: Condensed Matter 9 (4) (1997) 767.
[61] J. Hubbard, Electron correlations in narrow energy bands, Proceedings of the Royal Society of London. Series A. Mathematical and Physical Sciences 276 (1365) (1963) 238–257.
[62] Q. Feng, Electron correlation effect versus spin–orbit coupling for tungsten and impurities, Journal of Physics: Condensed Matter 32 (44) (2020) 445603.
[63] O. Hurtado-Aular, R. Añez, A. Sierraalta, Dft+ u study of the electronic structure changes of wo3 monoclinic and hexagonal surfaces upon cu, ag, and au adsorption. applications for co adsorption, Surface Science 714 (2021) 121907.
[64] Z. Shen, Z. Zhao, J. Wen, J. Qian, Z. Peng, X. Fu, Role of oxygen vacancies in the electrical properties of wo3- x nano/microrods with identical morphology, Journal of Nanomaterials 2018.
[65] X. Zhang, F. Tang, M. Wang, W. Zhan, H. Hu, Y. Li, R. H. Friend, X. Song, Femtosecond visualization of oxygen vacancies in metal oxides, Science advances 6 (10) (2020) eaax9427.
[66] J. Marian, B. Wirth, A. Caro, B. Sadigh, G. Odette, J. Perlado, T. D. de la Rubia, Dynamics of self-interstitial cluster migration in pure α-fe and fe-cu alloys, Physical Review B 65 (14) (2002) 144102.
[67] J. Marian, B. Wirth, G. Odette, J. Perlado, Cu diffusion in α-fe: determination of solute diffusivities using atomic-scale simulations, Computational materials science 31 (3-4) (2004) 347–367.

Appendix A. Summary of properties and evolution of tungsten oxides

Appendix A.1. Brief description of tungsten oxide phases

During oxidation of W, several different oxides may form. WO_3 is the most stable oxide, and at ambient temperature and pressure it displays a monoclinic structure consisting of a network of WO_6 octahedra (γ-WO_3). Above 330°C, WO_3 is seen to transform into an orthorhombic structure (β-WO_3), and tetragonal above 740°C (α-WO_3) [52]. WO_2 has a monoclinic structure in ambient conditions, and an orthorhombic structure at high temperatures and pressures. The crystal structure of monoclinic WO_2 also consists of WO_6 octahedra but with the difference that the

octahedra in WO_2 are edge-shared while they are corner-shared in WO_3 [48]. Between WO_3 and WO_2, the stoichiometric oxides $W_{18}O_{49}$ ($WO_{2.9}$), $W_{24}O_{68}$ ($WO_{2.72}$) have been reported at temperatures of 485°C and above [27, 53].

The intermediate phases $W_{18}O_{49}$ and $W_{24}O_{68}$ form due to the thermal stabilization of distorted arrangements of the WO_6 octahedra [54–56]. As the amount of chemical oxygen decreases, the usual corner-sharing arrangement of octahedra is partially replaced by groups of edge-sharing octahedra, which form pockets of shear planes. This is due to the tendency lattice to eliminate single oxygen vacancies by a crystallographic shear process [55, 56]. When these shears become coordinated, new stoichiometric lattices can form, e.g., $WO_{2.9}$ and $WO_{2.72}$. However, as revealed by the W-O phase diagram shown in Figure 1a [27], these phases have very narrow stability ranges close to the theoretical stoichiometry values. Interestingly, each phase is characterized by a distinctive color, as shown in Figure 1b, associated with the optical diffraction of the different octahedral arrangements.

Appendix A.2. Extraction of parabolic-to-linear transition thicknesses from tabulated experimental observations

To extract the critical scale thicknesses at which a transition from parabolic (protective layer) to linear (loss of protective layer) growth, we resort to the tabulated data given by Gulbransen *et al* [16] in a series of oxidation experiments at several temperatures and different oxygen atmospheres. The data are listed in Table A1 (units from the original paper have been updated to more current usage). The presumed phase is inferred from the observed color and the oxygen concentration (high O concentrations favoring WO_3 and low ones favoring WO_2). The oxide scale thickness at which a deviation from parabolic growth is observed is marked as the value of w^* to be used in the simulations.

The present model disregards the reaction kinetics between W and O. This is justified by the reaction rate being much faster than the diffusion rates. This can be quantitatively demonstrated by considering typical rates for the W-O reaction, e.g.: estimates, one can use a reaction constant given by the expression:

$$K_{\text{W-O}} = 6.1 \times 10^{23} \exp\left(-2.1/kT\right)$$

which gives the number of reactions per unit are per unit time in $[\text{cm}^{-2}\cdot\text{s}^{-1}]$ [57]. for an oxygen partial pressure of 49 Torr. At a temperature of 1500 K, this gives

Table A1: Transition oxide layer thickness calculated as a function of temperature at an O_2 partial pressure of 0.1 atm (adapted from ref. [16]). The observed color and presumed oxide phase are also included. The presumed phase is inferred from the observed color and the oxygen concentration (high O concentrations favoring WO_3 and low ones favoring WO_2). The mass density of metallic W is 19.3 g·cm^{-3}, which amounts to an atomic concentration of 6.3×10^{28} per m^3

T [°C]	w^* [μm]	observed surface color	presumed oxide
600	52	blue black	$WO_{2.72}/WO_2$
625	77	black with yellow spots	WO_3/WO_2
650	100	blue black with yellow covering	$WO_3/WO_{2.72}/WO_2$
700	155	blue black	$WO_{2.72}/WO_2$
750	181	black	WO_2
800	207	black	WO_2
850	310	black	WO_2
900	310	blue black	$WO_{2.72}/WO_2$
950	340	black	WO_2
1000	360	black	WO_2
1050	360	black	WO_2
1100	390	yellow black	WO_3/WO_2

5.5×10^{16} reactions per [cm^{-2}·s^{-1}]. When multiplied times ρ_W (assuming an O-rich environment), one gets approximately $\sim 10^{38}$ molecules of oxide per unit time per unit area. Compare this with diffusion-controlled oxygen fluxes obtained as $J_O = -D(\partial c/\partial x)$ with a diffusivity of 6.1×10^{-5} [cm^2·s^{-1}] at 1500 K in WO_2 (Table 2), which for a generic oxygen atomic concentration gradient of $\partial c/\partial x = 3.1 \times 10^{26}$ [cm^{-4}] (e.g., Fig. 5) yields fluxes of $\sim 10^{21}$ atoms per cm^2 per second. As the numbers show, the rate of arrival of oxygen to an interface is orders of magnitude slower than the reaction rate of oxygen with tungsten atoms. This substantiates the notion that oxygen transport is convincingly the rate limiting step of the oxidation process. Comment 1

Appendix B. Derivation of the Stefan equation

Mass conservation dictates that a discontinuity in the first derivative of the concentration at an interface, i.e., different arriving and exiting oxygen ion fluxes,

must be compensated by a moving interface. The rationale for such motion is provided by the conservation of the total oxygen concentration at the interface, which includes chemical oxygen (in the form of stoichiometric oxide phases) and free oxygen (free to diffuse through the crystal structure). At a given interface with a total area A, the amount of oxygen ions arriving per unit time from the left (negative side of the interface):

$$J_{\text{int}}^{-}A$$

The amount of oxygen ions exiting that same interface is:

$$J_{\text{int}}^{+}A$$

When both fluxes are equal, the interface is in equilibrium and does not move. However, if the the exiting flux is larger than the arriving flux, the interface must move lest there is a depletion in the total oxygen content. Such a gap must be filled by taking some of the exiting (free) oxygen and immobilizing it as chemical oxygen, i.e., growing the oxide layer. For a specific oxide phase with an oxygen-to-metal ratio of n, the number of oxygen ions needed to grow that phase by a thickness s is:

$$(sA)(n\rho_{\text{W}})$$

with the term (sA) indicating the volume of the new phase, and the term $(n\rho_{\text{W}})$ indicating the number of oxygen ions per unit volume needed to create the oxide phase. The rate form of the above expression is trivially:

$$\dot{s}An\rho_{\text{W}}$$

such that the excess flux exiting the interface is immobilized as stoichiometric oxygen. The balance equation is:

$$J_{\text{int}}^{-}A = J_{\text{int}}^{+}A - \dot{s}An\rho_{\text{W}} \tag{B.1}$$

which, after rearranging and eliminating the variable A becomes:

$$\dot{s} = \frac{J_{\text{int}}^{+} - J_{\text{int}}^{-}}{n\rho_{\text{W}}} \tag{B.2}$$

Appendix C. Electronic structure calculations

Appendix C.1. DFT+U method

The use of the DFT+U technique is necessary to reach a correct description of the electronic configuration of tungsten, which is critical to calculate formation energies and migration energy barriers [58]. Tungsten is a transition metal with electron configuration [Xe]$4f^{14}5d^{4}6s^{2}$, i.e., a partially filled d orbital that requires special DFT treatments [59].

When applying a one-electron method with an orbital-independent potential to transition metal compounds, one has as a result a partially filled d band with metallic type electronic structure and itinerant d electrons. This is definitely the wrong model for late-transition-metal oxides and rare-earth metal compounds where d (f) electrons are well localized and there is a sizable energy separation between occupied and unoccupied sub-bands (the lower Hubbard band and upper Hubbard band in a model Hamiltonian approach [60]). LDA/GGA functionals describe poorly the electronic properties of these localized orbitals and that is where DFT+U technique comes in. DFT+U accounts for electron-electron interactions in strongly correlated materials because the self-interaction error is dominant in d and f states.

DFT+U is based on Hubbard model, which solves the energy of electron correlation introduced or Coulomb repulsion between electrons at the same atomic orbitals [61]. The Hubbard model explains the transition between the insulation and conduction features of the systems with strong on-site repulsion using the following Hamiltonian:

$$H_{\mathrm{Hub}} = t \sum_{\langle i,j\rangle,\ \sigma} c^{\dagger}_{i,\sigma} c_{j,\sigma} + U \sum_{i} n_{i\uparrow} n_{i\downarrow} \tag{C.1}$$

The Hubbard Hamiltonian has two components, namely, the hopping integral t and the electron repulsion strength U. $c^{\dagger}_{i,\sigma}$ and $c_{j,\sigma}$ are the creation and annihilation operators of electron state at sites i and j and spin σ, respectively. The sum runs over all $\langle i,j\rangle$ nearest electron pairs, i and j. $n_i = n_{i\uparrow} + n_{i\downarrow}$ is the total density operator at site i.

The Hubbard model allows us to write the total energy of the system as a standard DFT energy plus a term representing the strong correlation of the electronic states in d (and f) orbitals.

$$E_{\mathrm{DFT}} + U[n] = E_{\mathrm{DFT}}[n] + E_{\mathrm{Hub}}[n_i^{\sigma}] - E_{\mathrm{dc}}[n_i^{\sigma}] \tag{C.2}$$

where $U[n]$ is the correction induced by DFT+U method, $E_{\mathrm{Hub}}[n_i^\sigma]$ is the Hubbard functional that describes the correlated states, and n_i^σ is the occupation number of the localized orbitals with the spin of σ and site i. The term of $E_{\mathrm{dc}}[n_i^\sigma]$ is a 'double counting' term, which is included because when we additively append the Hubbard term $E_{\mathrm{Hub}}[n_i^\sigma]$, the energy contribution of the related orbitals has already been counted in the DFT term. In our calculations we use a Coulomb interaction parameter of `LDAUU`=1.82 eV for pure metal W [62] because it does not affect the distribution of electrons for the attempt frequency calculations. However, we have also repeated the calculations with a value of `LDAUU`=6.2 eV used for WO_3 [63] and found only a change of 5% in the migration energy barriers.

Appendix C.2. DFT calculations of O diffusivity in WO_2

Tungsten is a transition metal with partially-filled d orbitals that requires special DFT treatments. Here we use the DFT+U technique with the parameterization for W used by Feng et al. [62]. The generalized gradient approximation (GGA) and Perdew-Burke-Ernzerhof (PBE) was applied to build the pseudopotential of the system and the frozen-core convention was implemented with the projector-augmented wave (PAW) method. The DFT simulations are performed with a cutoff energy of 600 eV and a k-point sampling of 2×2×4. The convergence criterion for the energy relaxation of the atomic positions was set to be 10^{-5} eV. Defect energies were calculated in a WO_2 supercell containing 36 atoms under constant volume.

Appendix C.2.1. Formation energy, E_f^{V} The calculations are based on supercells of $W_N O_{2N}$ lattices, where N is the number of W atoms. A vacancy is created by removing an O atom from a lattice position and placing it at infinity, i.e.:

$$E_f^{\mathrm{V}} = E_{\mathrm{W}_N\mathrm{O}_{2N-1}} + \mu_{\mathrm{O}} - E_{\mathrm{W}_N\mathrm{O}_{2N}}, \tag{C.3}$$

where $E_{\mathrm{W}_N\mathrm{O}_{2N-1}}$ and $E_{\mathrm{W}_N\mathrm{O}_{2N}}$ are the energy of the supercells with and without a vacancy, and μ_{O} is the chemical potential of an isolated oxygen atom. Under low oxygen partial pressures, μ_{O} satisfies:

$$\mu_{\mathrm{O}} = \mu_{\mathrm{O}_2} + \frac{1}{2} E^f_{\mathrm{WO}_2} \tag{C.4}$$

where μ_{O_2} is the chemical potential of bimolecular oxygen and $E^f_{\mathrm{WO_2}}$ is the formation energy of tungsten dioxide. For its part, $E^f_{\mathrm{WO_2}}$ is given by:

$$E^f_{\mathrm{WO_2}} = \mu_{\mathrm{WO_2}} - \mu_{\mathrm{O_2}} - \mu_{\mathrm{W}}$$

where the r.h.s. of the equation contains the chemical potentials (energy per molecule) of the perfect WO_2 crystal, bimolecular oxygen, and pure (metal) W. After carrying out the pertinent DFT calculations, we arrive at values of $\mu_{\mathrm{O}} = -7.65$ eV and $E^{\mathrm{V}}_f = 2.49$ eV. It must be kept in mind, however, that measurable concentrations of vacancies have been detected in tungsten oxide under ambient conditions [64, 65], which suggests that they exist in natural concentrations so as to naturally enable oxygen transport by a vacancy mechanism. This will the assumed mode of oxygen migration in WO_2.

Appendix C.2.2. Migration energy: E^{V}_m Migration energies are obtained using the *nudged elastic band* (NEB) method [44]. In the WO_2 crystal structure (monoclinic), there are three non-equivalent oxygen lattice positions, shown in Figure C1a and labeled as $\mathrm{V_{O_1}}$, $\mathrm{V_{O_2}}$, and $\mathrm{V_{O_3}}$. The NEB paths for the $\mathrm{V_{O_1}} \longleftrightarrow \mathrm{V_{O_2}}$ and $\mathrm{V_{O_2}} \longleftrightarrow \mathrm{V_{O_3}}$ migration trajectories are shown in Fig. C1. The resulting energy barriers are summarized in the following table:

Path	E^{V}_m [eV]
$\mathrm{V_{O_1}} \longrightarrow \mathrm{V_{O_2}}$	2.19
$\mathrm{V_{O_2}} \longrightarrow \mathrm{V_{O_1}}$	1.86
$\mathrm{V_{O_2}} \longleftrightarrow \mathrm{V_{O_3}}$	1.96

By way of comparison, an energy of 2.46 eV has been calculated for the $\mathrm{V_{O_1}} \longrightarrow \mathrm{V_{O_2}}$ path [48]. While all of these oxygen vacancy exchanges are viable diffusive transitions, here we take the $\mathrm{V_{O_1}} \longrightarrow \mathrm{V_{O_2}}$ as representative of all vacancy jumps and proceed to calculate the attempt frequency for that path.

Appendix C.2.3. Attempt frequency: ν_0 ν_0 can be obtained by resorting to harmonic transition state theory as [66, 67]:

$$\nu_0 = \frac{\prod_i^{3N} \omega_i^{\mathrm{eq}}}{\prod_i^{3N-1} \omega_i^{\mathrm{sp}}} \tag{C.5}$$

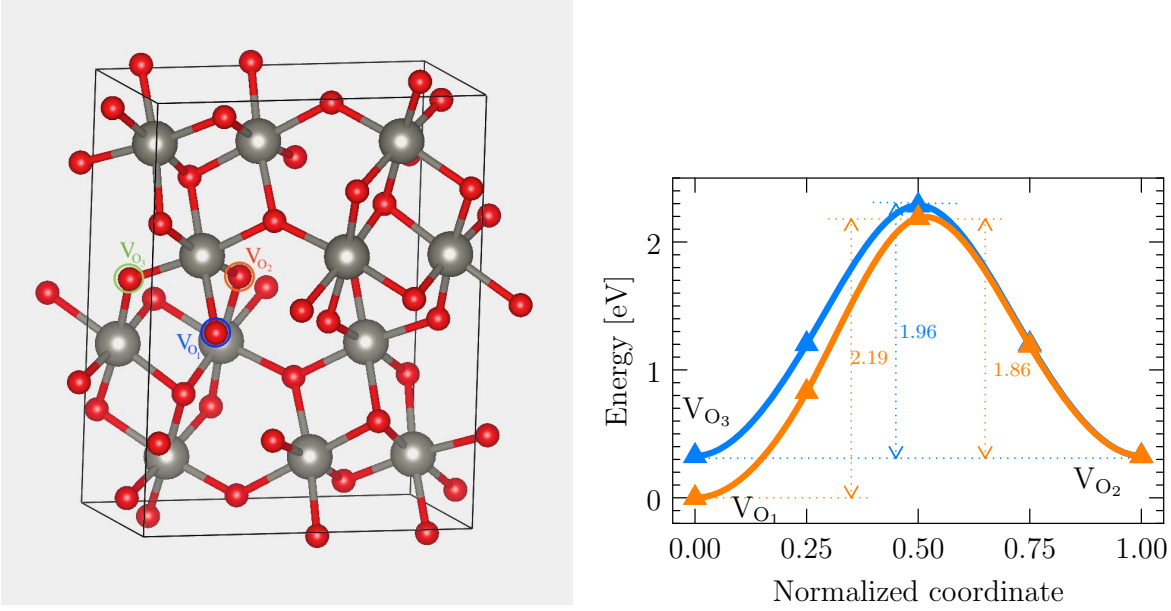

(a) WO_2 supercell (b) NEB calculations

Figure C1: (a) WO_2 supercell employed in the calculations. Red spheres symbolize O atoms, blue spheres W atoms. The three oxygen vacancy sites considered are marked and labeled. (b) Oxygen vacancy migration energy paths for the $V_{O_1} \longleftrightarrow V_{O_2}$ and $V_{O_2} \longleftrightarrow V_{O_3}$ trajectories.

where ω_i^{eq} and ω_i^{sp} are, respectively, the normal frequencies of vibration of the system at the equilibrium position (e.g., V_{O_1}) and saddle point of the migration path. In each case, the normal frequencies can be obtained by diagonalizing the *dynamical* matrix, $\boldsymbol{D}$, generated at the equilibrium and saddle point positions, which amounts to solving the eigenvalue problem defined by:

$$\boldsymbol{D\epsilon} = \boldsymbol{\lambda\epsilon}$$

where $\boldsymbol{\epsilon}$ is the eigenvector matrix and $\boldsymbol{\lambda}$ is a diagonal matrix containing all the eigenvalues of the system from which the eigenfrequencies can be calculated as $\omega_k = \sqrt{\lambda_{kk}}$. At the saddle point, one of the normal modes of vibration is undefined (imaginary eigenvalue) and eliminated from the product in the denominator of eq. C.5, hence the $3N - 1$ limit of the product.

The results for the $V_{O_1} \longrightarrow V_{O_2}$ path give a value of $\nu_0 = 243.2$ THz, which,

when inserted in eq. 11, results in $D_0 = 3.087 \times 10^{-5}$ $\mathrm{m^2{\cdot}s^{-1}}$. With this, the final expression for the oxygen diffusivity in WO_2 becomes:

$$D_4(T) = 3.087 \times 10^{-5} \exp\left(-\frac{1.9}{kT}\right) \quad [\mathrm{m^2 \cdot s^{-1}}] \tag{C.6}$$

These results are added to Table 2 to be used in the kinetic model simulations.